

# Study of Photons Orbital Angular Momentum for Optical Communications

André Cunha

*MEFT, Departamento de Física, Instituto Superior Técnico, Av. Rovisco Pais, 1049-001 Lisboa, Portugal*

The internet data traffic capacity is rapidly reaching the limits imposed by optical fiber nonlinear effects, having almost exhausted the available degrees of freedom needed to orthogonally multiplex data. Therefore the need urges to develop new methods in order to avoid the upcoming capacity crunch using classical communications channels. In this regard, recent results have suggested that the use of the orbital angular momentum (OAM) of photons as an additional degree of freedom is potentially unlimited in the number of achievable orthogonal states, therefore presenting itself as a possible major technological leap for future communication networks.

## I. INTRODUCTION & STATE OF THE ART

### A. Multiplexing & Modulation

Ingrained in the optical communications is the definition of orthogonality, which in a broad sense, means that if two of these dimensions are used to send two different signals, then it will be possible to distinguish them at the receiver without them impacting each other's detection. If these signals share a transmission medium, we refer to it as multiplexing. The method by which information is imprinted onto an optical carrier, and in its most broad definition, with the inclusion of coding to prevent transmission errors is referred to as modulation [1].

The currently available multiplexing techniques make use of several physical properties of light as shown in diagram 1. These techniques are Wavelength-Domain Multiplexing (WDM), Polarisation-Division Multiplexing (PDM), Coherent Wavelength-Domain Multiplexing (CoWDM), Orthogonal Frequency-Division Multiplexing (OFDM), Electronic Frequency-Division Multiplexing (ETDM), Orthogonal Time-Division Multiplexing (OTDM), optical Code-Division Multiple-Access (oCDMA) and Spatial-Domain Multiplexing (SDM). Regarding modulation, it is not that simple to categorise according to physical dimension without going into unneeded detail, but they can be summarised as On/Off Keying (OOK) and Pulse-Position Modulation (PPM) for amplitude, signal frequency for Frequency-Shift Keying (FSK) and Minimum-Shift Keying (MSK), polarisation for polarisation-Shift Keying (PolSK) and quadrature techniques involving both amplitude and phase for Quadrature Amplitude Modulation (QAM) and Quadrature Phase-Shift Keying (QPSK) respectively. All of these can be checked in detail in the work by Winzer [1].

### B. Evolution & Tendencies

In information theory, Shannon's source coding theorem establishes the limits to possible data compression, and the operational meaning of the Shannon entropy. In the history of optical communications, Shannon's the-

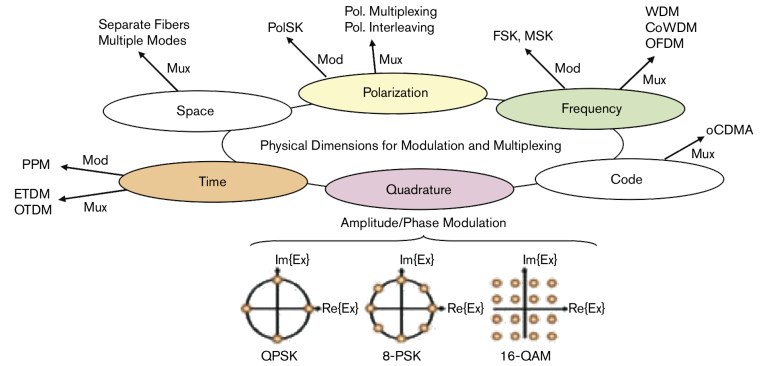


**Fig. 1:** Perspective diagram over multiplexing and modulation techniques according to physical dimension[1].

ory has established a behaviour and ceiling to expected evolution regarding spectral efficiency and the required SNR [2]. As it can be checked in the work by Winzer [1], Shannon's theory appears to provide a solid framework regarding the evolution of optical communications.

Despite an offset between reality and Shannon's curve [3], current optical communication technologies appear to be evolving as expected, although it can also be inferred that saturation may be near [1]. Adding to the fact that WDM capacity gains appear to be slowly diminishing while the number of WDM channels appears to be stagnant if imposing faster ETDM bit rates [1], new degrees of freedom must be found and exploited if improved capacities are expected.

It is in this regard that the Orbital Angular Momentum (OAM) may provide an improvement over existing technologies. OAM may reduce the offset from which current technologies are, relatively to Shannon's curve, catapulting optical communications to their expectable limits.

### C. Orbital Angular Momentum

A light beam can be described as a stream of photons. Each photon has an energy  $\hbar\omega$ , a linear momentum  $\hbar k$ , directed along the axis perpendicular to the wavefronts

and a *spin angular momentum* (SAM) of  $\hbar$  parallel or anti-parallel to the direction of propagation [4]. Less known is that light beams can also carry an *orbital angular momentum* (OAM) with no relation to polarisation and therefore also to photon spin [5].

**Result 1** (Laguerre-Gaussian Beam Modes).

$$\begin{aligned}
 U_{pl}(r, \varphi, z) = & \frac{C_{lp}^{LG}}{(1 + z^2/z_R^2)^{1/2}} \left( \frac{r\sqrt{2}}{w(z)} \right)^l L_p^l \left( \frac{2r^2}{w^2(z)} \right) \\
 & \times \exp \left[ \frac{-r^2}{w^2(z)} - \frac{ikr^2z}{2(z^2 + z_R^2)} \right] \exp(-il\varphi) \\
 & \times \exp \left[ i(2p + l + 1) \arctan \left( \frac{z}{z_R} \right) \right]
 \end{aligned} \tag{1.1}$$

The Laguerre-Gaussian (LG) beams, which have  $l$  intertwined helical wavefronts, are also valid solutions to the paraxial wave equation [6]. These beams are obtained by solving the paraxial wave equation in cylindrical coordinates  $r$ ,  $\phi$ ,  $z$  and are described by the result 1, where  $z_R$  is the Rayleigh range,  $w$  is the waist of the beam,  $k$  is the wavevector,  $p + 1$  is the number of annular regions,  $l$  is the number of intertwined helices and  $C$  is a normalization constant [6].

Defining the  $z$  component of the total angular momentum for LG modes in equation 1.2 [6].

$$M_z = \varepsilon_0 \mathbf{r} \times (\mathbf{E} \times \mathbf{B})_\phi = \frac{l}{\omega} |u|^2 \tag{1.2}$$

The linear momentum density per unit power for linearly polarised Laguerre-Gaussian beams is given by equation 1.3 [6].

$$\mathcal{P} = \frac{|u|^2}{c} \left[ \frac{rz}{(z^2 + z_R^2)} \mathbf{r} + \frac{l}{kr} \phi + \mathbf{z} \right] \tag{1.3}$$

If one divides  $M_z$  by the  $z$  component of the linear momentum density per unit power in equation 1.3,  $l/\omega$  is obtained [6]. The same result is obtained using the integrated physical quantities [7]. Imposing a single photon energy given by equation 1.5, one readily obtains  $l\hbar$  for the orbital angular momentum of a photon.

$$\frac{M_z}{\mathcal{P}_z c} = \frac{J_z}{P_z c} = \frac{l}{\omega} \tag{1.4}$$

$$E = \hbar\omega \tag{1.5}$$

For non-linearly polarised Laguerre-Gaussian beams, an additional component related to SAM appears in 1.2 [6]. The separation of the spin and orbital components of the angular momentum has been also derived for non-paraxial beams from the Maxwell's equations [8] and despite this rough approach to determine OAM per photon, OAM has been measured at the single photon level[9].

## D. OAM Generation

In the scope of optical communications systems, the available methods to generate OAM carrying beams are of great importance. In order to be able to explore OAM as a new degree of freedom, dynamic signal generation and control are required. Basically, OAM carrying beams are generated through a panoply of refractive and diffractive optical elements [10], Computer Generated Holograms (CGHs) and Spatial Light Modulators (SLMs). In this extended abstract we will focus on the SLM.

## E. Optical Communications Applications

Regarding fibers, current state of the art has recently achieved 1.6 terabit per second single core fiber capacity through OAM-WDM and specific fiber design. Data transmission was successful through more than 1 km long maintaining Bit Error Rate (BER) below the forward error correction Forward Error Correction (FEC) limit. In the same experiment, a OAM-PDM configuration allowed data transmission for also more than 1 km with a capacity of 400 gigabit per second. Detailed information available in the work by Bozinovic *et al.* [11].

Since OAM modes are more stable in free space, better results regarding aggregated capacity are usually the norm. However, as it can be expected, the research on these systems is still performed deeply in laboratory conditions with some disregard to distance [12, 13]. Nevertheless, the results regarding capacity are impressive and the state of the art appears to reach 0.1 Pbit/s aggregate capacity using 24 OAM modes across 42 wavelengths.

Another interesting application regarding OAM is in quantum communications and security. A quantum protocol known as 'quantum coin tossing' [9, 14] was implemented. In this particular protocol, OAM allows the use of qutrits offering an advantage over classical communication, and also over bidimensional quantum systems. This kind of protocol is of most of interest for applications where two partners wish to undertake a secure transaction, but do not fully trust each other.

OAM has the potential to improve aggregate system capacity through the offering of possibly a *unlimited* number of  $l$  modes. The current limitations regarding the inherent instability of these modes while combining them with established technologies such as WDM and PDM, if overcome, may allow OAM to be the next workhorse for optical communication systems in a world with ever-growing need for more aggregate capacity than ever and where more than ever, photonics technology imposes itself as the future communications.

## II. COMPUTATIONAL ASPECTS

In order to enable our experiment, some computational work is required in two different fronts. First, we will

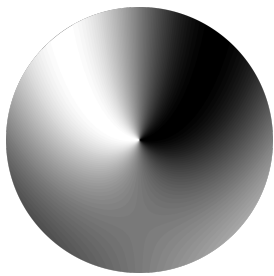


**Fig. 2:** Pure spiral vortex  
 $l = -1$ .

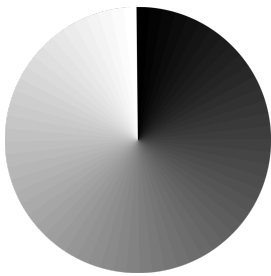


**Fig. 3:** Linearized spiral  
vortex  $l = -1$ .

need to provide some code to be able to generate the phase patterns which we will load in our SLMs in order to shape our wavefronts. Second, we will want to simulate the propagated field after the SLM interaction as a control method to our methodology. As an additional simulated experience, we will try to demodulate a spiral phase CGH OAM beam.

### A. Phase Pattern Generation

Before proceeding, we have to distinguish the differences between the two approaches that were used to shape our OAM carrying beams. SLM beam shaping consists of imposing a certain phase pattern in the LCoS SLM. In order to generate phase shaped LG beams, the pattern may be the phase profile of the interference of a certain LG beam with a Gaussian beam. For  $LG_{-1}^0$ , the spiral phase is shown in figure 2. This complex phase is unnecessary for our purposes. The essential feature which allows for OAM creation resides at the center of the spiral. This way, in order to achieve our purpose, it suffices to generate a simpler phase profile as shown in figure 3. This procedure is standard regarding not only but also the optical communications applications of OAM as it can be seen in the work by Wang *et al.* [12] and Bozinovic *et al.* [11]. The final image may be described as a grayscale matrix  $m \times n$  which obeys the equation 2.1.

$$T(m, n) = T_0 \pmod{(\theta l, 2\pi)} \quad (2.1)$$

In this equation,  $\theta$  is the polar angle,  $l$  is the topological charge and  $T_0$  is an adjustment parameter only relevant if we want to create superpositions which we won't be using. This method is often referred as spiral phase shaping.

The forked diffraction, despite different, it is actually based in the former one. In the previous method, it appears to be experimentally challenging to ensure precision of the generated OAM beam since the Liquid Crystal on Silicon (LCoS) SLM is a reflective device which will always reflect some unmodulated Gaussian component of the original beam. Since OAM modes are much less intense than the Gaussian component, the final beam will be affected. In order to address this difficulty, by com-

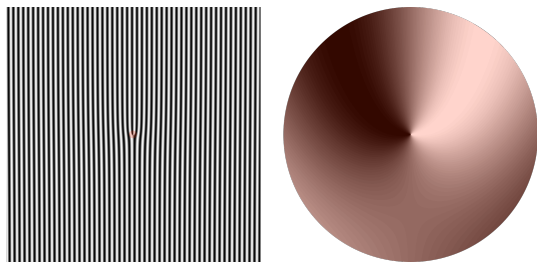


**Fig. 4:** Forked diffraction pattern with  $l = 1$  on the left.  
Vortex which provides OAM zoomed in in the right.

binning the former spiral phase pattern in its approximate form with a standard linear diffraction pattern, the OAM modes may be separated in different angles as it shall be demonstrated further on. Again, if we consider a  $m \times n$  grayscale matrix, this combination may be described by the following equation.

$$T(m, n) = T_0 \cdot \exp \left[ \alpha \cdot li \cdot \cos \left( \theta \frac{l}{2} - \frac{(2\pi r \cdot \cos \theta)}{G} \right) \right]$$

More complex than the first equation, this equation parameters has the same and some additional ones:  $G$  controls the fringe spacing through what can be interpreted as a scale factor around the singularity. Examples shall be presented further on, along with propagation simulations. Again, the essential feature in this pattern is the center of the image where the singularity takes place. Given its form, this patterns are frequently referred as forked diffraction patterns or, opposed to the former method, unaligned spiral phase shaping.

### B. Propagated Field Simulations

A simple simulation of the propagated field was developed in order to predict some results and as a control method of our experiment. The algorithm used is a direct implementation of the Fresnel diffraction approximation.

**Result 2** (Fresnel Diffraction Approximation).

$$\begin{aligned} U^{out}(x_2, y_2) &= \iint_{-\infty}^{+\infty} U^{in}(x_1, y_1) \cdot h(x_2 - x_1, y_2 - y_1) dx_1 dy_1 \\ &= U^{in}(x_1, y_1) * h(x_1, y_1) \end{aligned}$$

$$h(x_1, y_1) = \frac{\exp(ikz)}{i\lambda z} \exp \left[ \frac{ik}{2z} (x_1^2 + y_1^2) \right]$$

This choice was made because the direct implementation of the angular propagation method is extremely complex. Therefore, it is unreasonable to follow such path in this comprehensive work. Also, the Fresnel approximation for diffraction seems to be the standard approach in

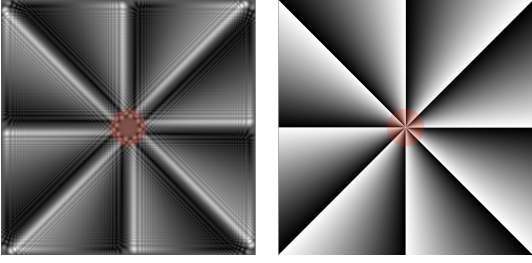


**Fig. 5:** Propagation simulation for  $l = -8$  spiral CGH on the left and original phase CGH on the right (the phase CGH represents the optical field, not the SLM phase pattern). The OAM optical vortex is signaled in red on the left and the incidence is signaled in red on the right.<sup>1</sup>

these cases, although its implementation may be more or less refined [12].

Following the result 2, the expression can be further simplified by writing it in the form of the following equation.

$$U^{out}(x_2, y_2) = \mathcal{F}^{-1} \{ \mathcal{F} \{ U^{in}(x_1, y_1) \} \cdot H(\nu_{x_1}, \nu_{y_1}) \}$$

Function  $H$  presented in the equation below, and is the transfer function valid for the Fresnel diffraction approximation and is obtained from the Fourier transform of the Fresnel diffraction approximation impulse  $h$  shown in result 2.

$$H(\nu_{x_1}, \nu_{y_1}) = \mathcal{F} \{ h(x_1, y_1) \} = \exp(ikz) \cdot \exp[-i\pi\lambda z(\nu_{x_1}^2 + \nu_{y_1}^2)]$$

Our algorithm implements this approach. Its input is a starting optical field which we want to propagate. The input will correspond, to the phase pattern imposed in our Gaussian beam. We also assume the original pattern to propagate is the modulated phase of the beam at the SLM. The implemented routine allows for input of the laser wavelength  $w$ , the complex amplitude of the starting optical field  $U_0$  and  $L_0$  which is the width of the starting optical field plane. Then, the sampling theorem is applied suggesting the maximum distance allowed for diffraction according to Picart and Li [15] expressed as  $z_{max} = L_0^2 / \lambda w$  (where  $\lambda$  is the biggest size of the pixelated matrix), suggested maximum value for the diffraction plane distance  $z_0$ .

Regarding modulation for multiplexing, three tests were performed using three different phase patterns in the same physical conditions: wavelength  $w = 633\text{nm}$ , diffraction plane distance  $z_0 = 100\text{mm}$  and width of the starting field  $L_0 = 9\text{mm}$  (the width of the SLM matrix). Both spiral and fork CGHs were propagated with a value of  $l = -8$  for the former and  $l = -2$  for the latter. Inverse phase patterns produce similar results, although inverted. The starting patterns and their respective propagation are presented in figure 5 for the spiral phase CGH

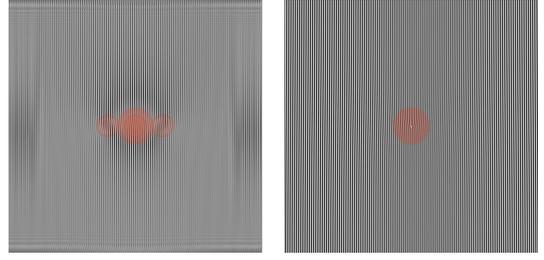


**Fig. 6:** Propagation simulation for  $l = -2$  fork CGH ( $l = 2$  on the left and  $l = -2$  on the right) with  $G = 15$  (4 px per fringe which is about  $40\mu\text{m}$  in our SLM) on the left and original phase CGH on the right. The OAM optical vortices are signaled in red in the left and the incidence is signaled in red on the right.<sup>1</sup>

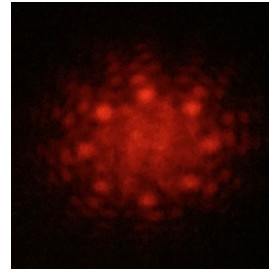


**Fig. 7:** Long distance propagation photo for projected  $|l| = 8$  spiral CGH using the setup shown in figure 12 without a polariser.



**Fig. 8:** Long distance propagation photo for  $|l| = 2$  fork CGH with  $G = 15$  (4 px per fringe which is about  $40\mu\text{m}$  in our SLM) using the setup shown in figure 12.

and figure 6 for forked diffraction CGH<sup>1</sup>.

In order to try to simulate OAM spiral phase CGH demodulation, a simulated experience using two configurations was done: a composition of a propagated OAM  $l = 8$  beam and an inverse spiral phase CGH was made using imaging software and contrast adjustments were made to diminish aliasing effects on the former. As a control subject, the same was done but changing the second phase pattern to one equal to the original one. Both situations assume the viewer is behind the beam, and we want to propagate the spiral beam through two inverse SLM phase CGHs configurations. Because of this assumption, the color scale significance is inverted in this particular simulation (black for 0 and white for  $2\pi$ ). The resulting images were propagated in the simulation and both results were filtered from aliasing using equal parameters. Results are presented in figures 9 and 10.

<sup>1</sup> The red circle spots in the original phase patterns are also an approximated representation of the beam we expect to use, having a diameter of about 15 px, the phase patterns were made to fit the SLM with a width of 1024 px which by assuming a pixel size of  $9\mu\text{m}$  translates into 1.35 mm which is close to the value of 1.2 mm we expect to use.

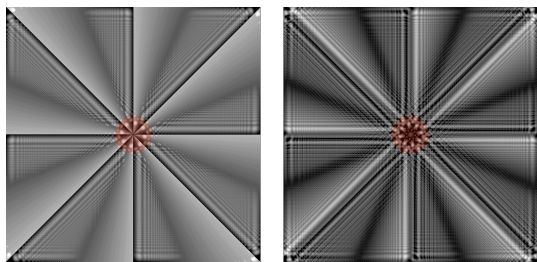


**Fig. 9:** Composition for  $l = -8$  spiral beam and  $l = 8$  phase CGH on the left and its propagation on the right. The OAM optical vortex is signaled in red on both sides.<sup>1</sup>

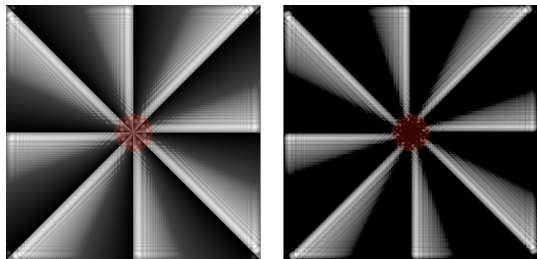


**Fig. 10:** Composition for  $l = -8$  spiral beam and  $l = -8$  phase CGH on the left and its propagation on the right. The OAM optical vortex is signaled in red on both sides.<sup>1</sup>

The pixelation of the final results is probably related to aliasing but also to the use of fast Fourier transform algorithms instead of more refined implementations of the Fourier transform. Regarding the spiral diffraction CGH propagation, the result appears quite in agreement with the early results obtained in the laboratory by direct observation of intensity due to amplitude-phase coupling effects present in Twisted Nematic Liquid Crystal (TN) technology [16]. Regarding the forked diffraction CGH propagation, in our theoretical approach we always assumed the premise of very small angles in the diffraction problem. The pattern of unaligned spiral phase shaping, actually diffracts in angles which are significant. However, despite these issues, the actual result is surprisingly good. A central maximum can be clearly seen in the propagated field. Additionally, the symmetrically charged OAM beams vortices can be easily seen where they should appear (see figure 6).

As for the demodulation attempt, this simulation was performed as a trial. Some pre-processing and post-processing was needed in order to improve the results. The contrast of the original OAM beam was enhanced using imaging software and fixed parameters in both situations. Then, the beam was composed with an unaltered inverse phase pattern and another beam was composed with an identical phase pattern. Both compositions were propagated. In order to reduce aliasing, fixed parameter contrast adjustment was performed in both results in order to eliminate aliasing effects. The results are quite in agreement with what we expect: the inverse phase pattern recovers some of the original phase while the the

identical one maintains the singularity. However, given the rather heavy pre and post-processing processes involved, without strict quantitative control measures, the result could be a coincidence. However, the adjustments made through contrast are not without relation to our real life setup: dynamic range limitations and the phase modulation limit of  $0.8 \cdot \pi$  express themselves in adjustments of contrast in imaging which remove gray levels, which is equivalent to a reduced dynamic range. It should be added that the adjusted propagation simulations are actually more resemblant with real life results than the originals which is quite in agreement with the former assessment.

### III. EXPERIMENTAL SETUP

Before proceeding to the proper methodology description it is important to introduce a vital element of our experiment setup: the SLM. There are several types of LCoS SLMs but most of them rely on the application of an electric field to a Liquid Crystal (LC) substrate contained by optical surfaces [16, 17]. Several factors regarding speed and efficiency condition these devices which summarize into two important parameters: spatial resolution and frame rate [16]. For our purpose, a good spatial resolution is paramount since we are concerned about efficiency since in principle, we wish only to multiplex information in order to be able to use a future OOK modulation scheme which requires only a fixed configuration in time.

Naturally, the first and biggest distinction between LC SLMs are the LCs used to modulate the light: ferroelectric, TN and Parallel Aligned Nematic Liquid Crystal (PAN) LCs. Other LC applications do exist despite those presented in this thesis [18], but these are the most typical [17].

In this extended abstract, TN technology will be our main focus regarding LCs since our equipment of choice is based on this technology. In TN-LC SLMs, the LCs start aligned in a helix pattern across each pixel cell like it is shown in figure 11. By applying a certain voltage, the molecules start to align with the field breaking the aforementioned pattern allowing adjustable phase modulation.

The phase retardation associated to LCs is shown in the integral 3.1 result [16, 18–20]. Therefore TN-LCs allow phase retardation as a function of voltage while allowing fast switching and some dynamic range.

$$\delta = \frac{\pi}{\lambda} \int_{z=0}^{z=2d} \Delta n(z) dz = \frac{2\pi d \Delta n}{\lambda} \quad (3.1)$$

Several factors may condition the functioning of the SLMs. These factors are diffraction efficiency, fill factor, aliasing, reflectivity or transmittance, angle of incidence, thickness, voltage control and temperature.

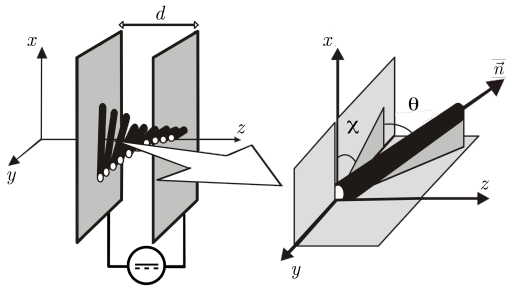


**Fig. 11:** Twisted Nematic Liquid Crystal LC pixel cell detailing  $\vec{n}$ , tilt angle  $\theta$  and twist angle  $\chi$  [16].

Our equipment of choice is a LCoS TN SLM SDE1024 by Cambridge Correlators. State of the art SLM OAM beam generation for optical communications usually use PAN technology [11, 12]. However, OAM beam generation for optical tweezers applications have long been using TN technology [17]. Regarding possible issues of diffraction efficiency associated with TN technology, assuming a maximum value of  $0.8\pi$  and OAM beam generation through the usage of a  $0$  to  $2\pi$  unaligned spiral pattern, [17] refers that the beam is attenuated only in its diffraction orders as it should, since the unmodulated component should simply reflect aligned. Regarding aligned spiral patterns, even limited by a rather low dynamic range, partial phase modulation may be enough to generate optical vortices carrying OAM which is enough considering our objectives. Full phase modulation or demodulation are not a possibility with these technical limitations, although it is expected that at least a partial modulation and demodulation are possible by using these equipments. It should be noticed that despite that OAM is usually associated with integer values of  $l$ , fractional values of  $l$  are also possible [21].

As a final remark regarding the choice of the SLM, state of the art PAN SLMs are expensive costing thousands of euros while low cost TN-LCoS SLMs equipments are about one thousand euros each. This is a rather important limitation since our budget is very limited.

### A. OAM Modulation for Multiplexing

The setup for OAM carrying beams generation is similar in broad terms in the three cases: we use a 5 mW 632.8 nm HeNe laser Melles-Griot 05-LHR-151, expand it to about 1.2 mm diameter from 0.8 mm maintaining the collimation of the beam and incise it in the active area of the SLM. This is done through a set of mirrors in order to minimize the angle of incidence in the SLM and the beam expander uses two lenses of 100 mm and 150 mm. After the incidence in the SLM, the beam is registered through a Phasics SID4 CCD-WFS (in order to measure phase profiles for OAM carrying beams, since the device imposes a Gaussian form to the phase,

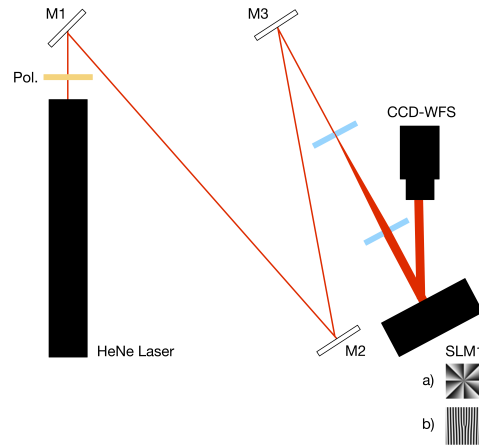


**Fig. 12:** Setup for modulating an OAM beam for MUX.

residual phase measurement must be used). This modest beam expansion was the maximum available since, despite having a 4.8 mm by 3.6 mm aperture in the CCD-WFS, OAM carrying beams are shaped like rings much larger than the original beam, whose radius increases proportionally to the absolute value of  $l$ . On the other hand, it is crucial to expand the beam in order to maximize the relative size of the modulated beam versus the unmodulated components which arise due to aliasing and reflectivity while easing the alignment. It was also observed that, the SLM had more difficulty in modulating a thinner beam, perhaps due to superior photon density. As a final remark regarding the input Gaussian beam calibration, despite great care used to calibrate the beam, during the evolution of the experiment using several spiral phase patterns with different values of  $l$ , and even during the demodulation attempts, two main factors proved to be much more relevant than the Gaussian quality of the input beam: alignment and collimation. Assuming a pixel size of  $10\ \mu\text{m}$  adding  $1\ \mu\text{m}$  to the reference value in order to compensate for grid spacing, a beam diameter of 1.2 mm and assuming the beam is collimated, and provided that OAM modes expand according to the LG beam diameter dependence on  $l$  expressed in equation 3.2 Padgett *et al.* [22], for the most used configuration of  $l = 8$  we expect a ring of about 2.4 mm to the maximum intensity. Since the ring overflows from the maximum intensity point, about 3 mm total diameter is perhaps a good estimation. Since the CCD-WFS has a pixel size of about  $30\ \mu\text{m}$ , an image of about  $100 \times 100$  px is a likely result.

$$d_{LG}(I_{max}) = \sqrt{2|l|}w(z) \quad (3.2)$$

For spiral phase CGH, while following the basic setup described above, the first approach consists in using a horizontally polarised beam as an optical input signal. In order to achieve this, a polarising beam splitter is used at the output of the HeNe laser following the schematic in figure 12.

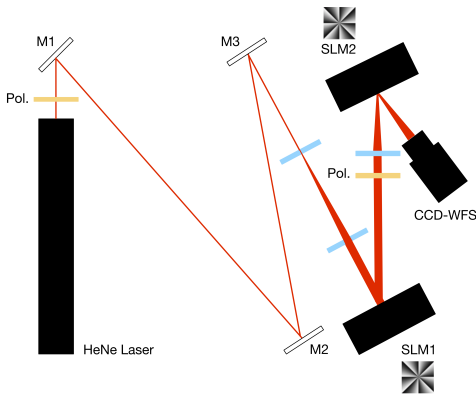


**Fig. 13:** Setup for demodulating an OAM beam for DEMUX (inverted mask shown in SLM 2 for illustration purposes).

The spiral phase CGH using a elliptically polarised beam approach actually resulted from an unexpected effect due to unproper equipment. The introduction of ellipticity in the polarisation had an unforeseen effect on the modulation of the beam using a TN-LC SLM. After some research, a setup loosely based on the work of Pezanti and Chipman [23] and Moreno *et al.* [24], which uses a setup involving a polariser with a Quarter Wave Plate (QWP) was tested.

Finally, the last approach uses forked diffraction CGH and linear polarisation. Regarding the setup, the general approach described above was used, using a polariser in order to obtain a linearly polarised beam. In order to validate the simulation, several adjustment parameters were tested and the simulation, despite its limitation proved itself as good method to chose working values for the parameters of the fork diffraction CGH.

## B. OAM Demodulation for Demultiplexing

For the second part of the experiment, the modulated spiral phase shaped linearly polarised OAM beam should be back-converted to a Gaussian beam at least partially. The intensity singularity present in OAM beams should be replaced by a recognizable peak of intensity. In order to achieve this, another SLM is needed where an inverse  $-l$  spiral phase CGH is loaded in order to cancel the spiral imprint which generates the OAM. Correct alignment is very difficult since it is needed in both orthogonal and polar coordinates in order to be able to rotate the SLM to adjust the spiral alignment optimizing the experiment. In order to achieve this, a ThorLabs cage system was used to hold the second SLM. Additionally, recalling the first beam expansion which is then followed by a OAM modulation which further increases the size of the ring, since our beam is now outside the diffraction region, the use of a 35 mm lens was needed at the input (in the cage mount) of the second SLM to optimize the back conversion process. The lens was placed in a position where the

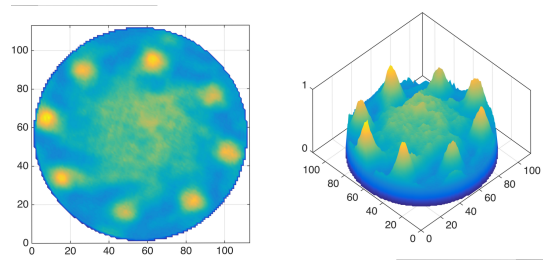


**Fig. 14:** Normalized intensity profile for a  $l = 8$  OAM beam (linearly polarised input beam and  $l = 8$  spiral phase CGH generated on SLM 1 and reflected on turned off SLM 2).

beam is reduced, but big enough to be able to be modulated. From an operational standpoint, about 30 mm was found to be the optimum distance enabling a quick reduction while allowing the measuring of the demodulated signal at a possible operational distance regarding the cage mount and the size of the CCD-WFS. Since the beam suffers size alteration through an optical component, while the theory states it shouldn't be affected it is consistent with our visual analysis and measured data.

Additionally, a control test was conceived. The test is simple but quite clear: since the back conversion will be far from ideal due to the limitations of the SLM, and since the original spiral phase CGH generated beams possess some degree of noise in the center region, it is important to diminish the possibility that a peak might be related to noise rather than phase demodulation. Disconnecting the demodulating SLM doesn't erase this possibility since the LC randomized helix pixel matrix will cause unpredictable effects on the input signal. Therefore, the way found was simply to load an identical spiral phase CGH which may have one of two results: assuming an inverse spiral phase CGH, it should result in a measurable central peak, if despite its pattern, the identical one also generates a peak, then, our experiment is at best inconclusive. On the other hand, if the residual intensities at the beam are modulated resulting in an improved intensity singularity, we can safely discard the possibility of the desired peak being noise.

## IV. RESULTS

### A. OAM Modulation for Multiplexing

The intensity results for a  $l = -8$  spiral phase CGH (which generates a  $l = 8$  OAM beam) using both randomly polarised light and linearly polarised light are within the expected. The quantity of unmodulated light is clearly visible in both cases but the introduction of a polariser visibly improves this issue. The intensity results clearly show the expected amplitude-phase coupling effects for TN technology where the intensity follows the phase profile. The obtained intensity profile despite being annular, the ring is made of intensity peaks instead of

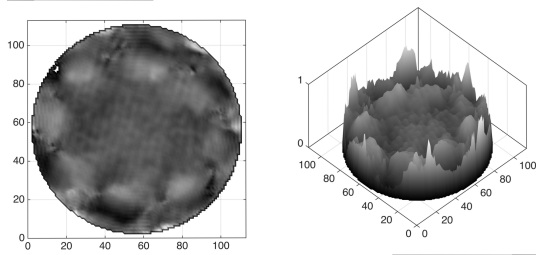


**Fig. 15:** Normalized phase profile for a  $l = 8$  OAM beam (linearly polarised input beam and  $l = 8$  spiral phase CGH generated on SLM 1 and reflected on off SLM 2).

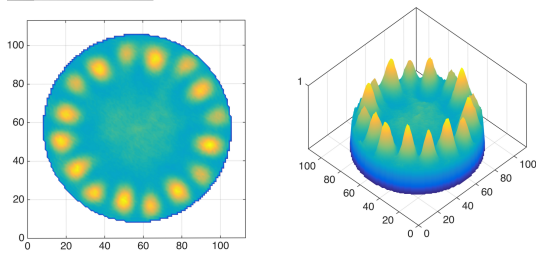


**Fig. 16:** Normalized intensity profile for a  $l = 8$  OAM beam (elliptically polarised input beam and  $l = -8$  spiral phase CGH.)

a smooth constant intensity ring as it is usually obtained by using PAN technology [12]. The limited phase modulation capability of our equipment, typical of TN SLMs, also helps to justify this result. The profile figures for this results aren't published in this extended abstract, but similar conclusions can be seen by turning the SLM 2 off in the demodulation setup (see figures 14 and 15).

Regarding the elliptically polarised input beam, the intensity profile in figure 16 suggests improved phase modulation since the profile is closer to a ring and the quantity of unmodulated light is reduced. However, through the analysis of the wavefront of this beam, the profile in figure 17 seems to indicate an  $|l| = 16$  wavefront which is strange. Closer inspection suggests some kind of phase disruption on each ramp of what we would want to be 8 smooth ramps and ends up looking like 16 ramps. Work on polarisation eigenstates by Pezzaniti and Chipman

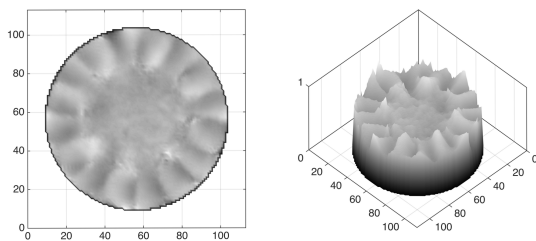


**Fig. 17:** Normalized phase profile for a  $l = 8$  OAM beam (elliptically polarised input beam and  $l = -8$  spiral phase CGH.)

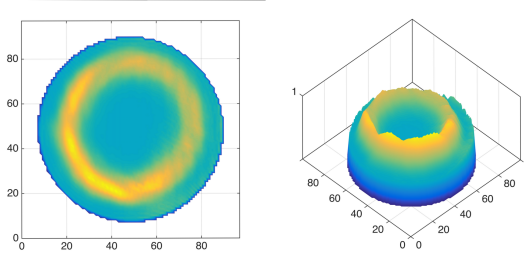


**Fig. 18:** Normalized intensity profile for a  $l = -1$  OAM beam (linearly polarised input beam and  $|l| = 1$  forked diffraction CGH.)

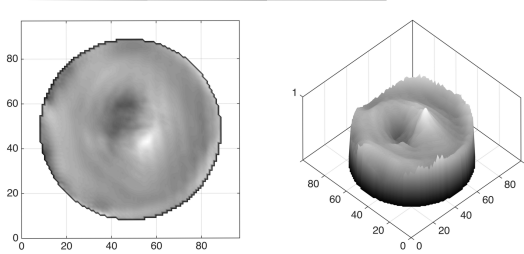


**Fig. 19:** Normalized phase profile for a  $l = -1$  OAM beam (linearly polarised input beam and  $|l| = 1$  forked diffraction CGH.)

[23] and Moreno *et al.* [24] suggests that TN technology phase modulation may be improved.

What appears to be the best result regarding OAM beams purity is obtained through forked diffraction CGHs since they possess a true vortex singularity and through diffraction, unmodulated light gathers at the 0<sup>th</sup> order beam. By using a  $|l| = 1$  forked diffraction CGH to generate a pair of  $l = 1$  and  $l = -1$  OAM symmetric beams, the measured intensity of the  $l = -1$  beam in figure 18 is an almost perfect shaped ring despite a some mplitude-phase coupling effects. The wavefront shape in figure 19 is also very good, resembling to a spiral ramp surrounding a singularity. The effect of limited phase modulation capabilities of TN technology should exist between the maximum and minimum phase difference in the wavefront shape. Again, the simulation was very good predicting this result.

Before proceeding to a OAM carrying beam demodulation, a  $l = 8$  spiral phase CGH was loaded in the first SLM while maintaining the second SLM turned off (using always linearly polarised light). The result for intensity shown in figure 14 shows increased noise, probably induced by random modulation effects generated by the LC matrix but also beam deformation related to the angles of incidence and the lens used in the second SLM. Along with the increase of the noise, the random modulation effects are also visible because of the reduction of the intensity of the modulated peaks. Regarding the phase profile shown in figure 15, we can see that the wavefront modulation is maintained. Given this result, this result is unsuitable to use as a reference beam for our final result,

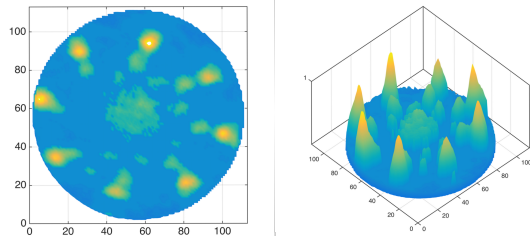


**Fig. 20:** Noise filtered normalized intensity profile for a  $l = -8$  OAM demodulated beam (linearly polarised input beam and  $l = 8$  spiral phase CGH generated on SLM 1 and demodulated on SLM 2 with  $l = 8$  spiral phase CGH).

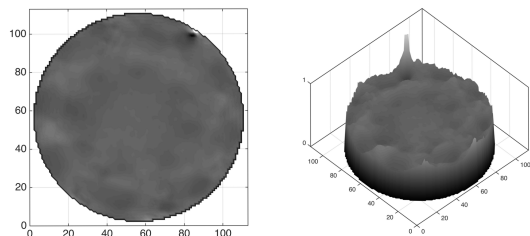


**Fig. 21:** Normalized phase profile for a  $l = -8$  OAM demodulated beam (linearly polarised input beam and  $l = 8$  spiral phase CGH generated on SLM 1 and demodulated on SLM 2 with  $l = 8$  spiral phase CGH).

regarding noise considerations.

## B. OAM Demodulation for Demultiplexing

Proceeding to OAM demodulation, since we use a reflective SLM and considering that OAM charge flips with reflection, a  $l = 8$  spiral phase CGH was loaded in the first SLM generating a  $l = -8$  beam. Then, a complementary  $l = 8$  spiral phase CGH was loaded on the second SLM.

The results for both noise filtered intensity and phase are shown in figures 22 and 23 respectively. Regarding phase, the result is quite satisfactory. Recalling that we

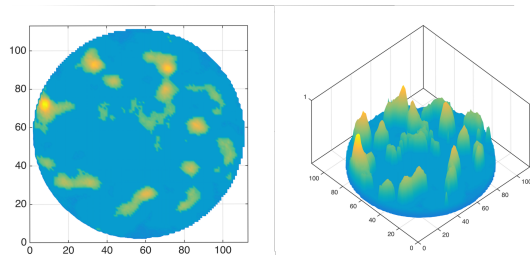


**Fig. 22:** Noise filtered normalized intensity profile for a double modulated  $l = -8$  OAM beam (linearly polarised input beam and  $l = 8$  spiral phase CGH generated on SLM 1 and remodulated on SLM 2 with  $l = -8$  spiral phase CGH).

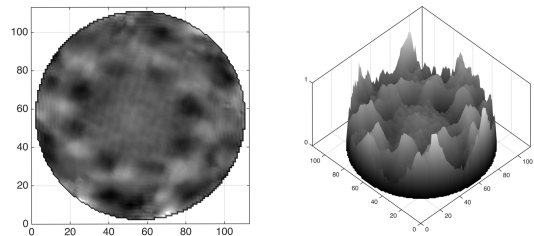


**Fig. 23:** Normalized phase profile for a double modulated  $l = -8$  OAM beam (linearly polarised input beam and  $l = 8$  spiral phase CGH generated on SLM 1 and remodulated on SLM 2 with  $l = -8$  spiral phase CGH).

measure residual phase effects considering a Gaussian beam reference, the residual phase for this beam is almost nonexistent and only an almost flat ring trace can be seen. Recalling the simulation, it should be noticed that if the wavefront at the core in fact resembles a Gaussian or cylindrical profile, it is promptly removed since we only look for the residual phase profile.

In order to try to improve the comprehension of this results regarding noise, and as referred previously, a control test was devised as previously described. So, after the introduction of a  $l = -8$  spiral phase CGH in the second SLM the results for both noise filtered intensity and phase are shown in figure 22 and 23 respectively. The raw result for intensity was considered unclear and it is not presented.

Regarding the phase profile shown in figure 23, the result is quite clear. Unlike the standard demodulation where an almost flat profile is obtained, here we have an increased modulation behaviour, since the peaks are not only clearer than the standard demodulation, but more pronounced than those of a standard OAM beam generated with this setup as shown in 15. Naturally, this translates itself as a stronger intensity singularity in the core. Regarding the simulation shown in figure 9, it appears to be concordant given the enhanced phase peaks shown in the simulation.

Finally, in order to clarify the obtained intensity results for both the standard demodulation and the control test, an equal noise filter was applied in the data in order to enhance any hidden significance since the intensities are very weak. The results for the standard demodulation and the control test are shown in figures 20 and 22 respectively. After applying the noise filter, our phase analysis conclusions are proven. The standard demodulation actually shows a central peak surrounded by a smaller vortex ring related to the reversal of the phase modulation which can also be seen, if we assume amplitude and phase coupling, in the simulation in figure 10. By opposition, the core of the control test intensity is almost flat, and the visible intensities are clearly due to inhomogeneities of the beam. The profile is far from clear, but the superposition of the peaks predicted in the simulation in figure 9 is also identifiable.

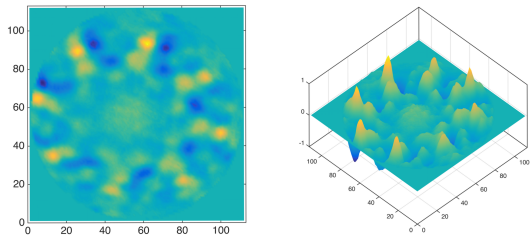


**Fig. 24:** Normalized intensity profile for the subtraction of the demodulated  $l = -8$  OAM beam by the double modulated  $l = -8$  OAM beam.

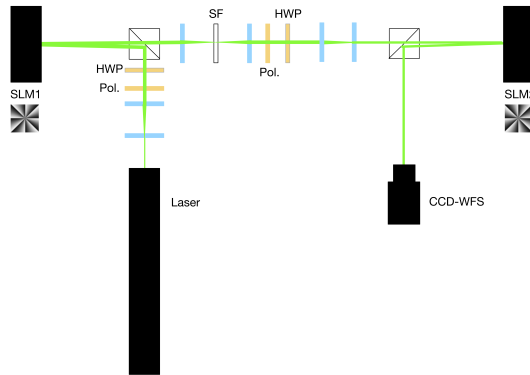


**Fig. 25:** Improved setup for demultiplexing schematic (inverted mask shown in SLM 2 for illustration purposes).

As a final test, both the original raw intensities for both the standard demodulation and the control test were subtracted in order to identify the noise and systematic inhomogeneities and the result is shown in figure 24. The result solidifies what we already saw in the former analysis. There's a clear local maximum at the core as expected through the demodulation of a OAM beam, and the effects of systematic inhomogeneities and noise common to both profiles is diminished. The core profile is in complete agreement with the simulation shown in figure 10, again assuming amplitude-phase coupling.

## V. FINAL REMARKS

The corner stone of the proposal of this work was to establish a foundation for the study of the OAM of photons applied to optical communications. In order to achieve this, a rather comprehensive approach was chosen in order to connect the several areas of study that provide the technical and human motivation for this work.

All and all, we end this work with a sense of accomplished mission, we think that any work that may follow, either more related to physics or optical communications has here a good starting point and we hope that this work helps to seed interest in the study of the fascinating world of twisted light and its applications.

As a final remark, and summing some of the sugges-

tions made throughout this work, an improved setup for demodulation is proposed (see figure 25). This setup addresses some of the issues regarding angle of incidence, beam cleaning, wavelength reduction and polarisation control.

- [1] P. J. Winzer, IEEE Leos Newsletter (2009).
- [2] C. E. Shannon, SIGMOBILE Mob. Comput. Commun. Rev. **5**, 3 (2001).
- [3] P. J. Winzer and A. H. Gnauck, *112-Gb/s polarisation-multiplexed 16-QAM on a 25-GHz WDM grid* (Proc. ECOC, 2008).
- [4] R. A. Beth, Phys. Rev. **50**, 115 (1936).
- [5] M. J. Padgett and L. Allen, Contemporary Physics **41**, 275 (2000).
- [6] L. Allen, M. W. Beijersbergen, R. J. Spreeuw, and J. P. Woerdman, Physical review. A **45**, 8185 (1992).
- [7] J. P. Torres and L. Torner, *Twisted Photons*, Applications of Light with Orbital Angular Momentum (John Wiley & Sons, 2011).
- [8] S. M. Barnett and L. Allen, Optics Communications **110**, 670 (1993).
- [9] G. Molina-Terriza, J. P. Torres, and L. Torner, Nature Physics **3**, 305 (2007).
- [10] A. M. Yao and M. J. Padgett, Advances in Optics and Photonics **3**, 161 (2011).
- [11] N. Bozinovic, Y. Yue, Y. Ren, M. Tur, P. Kristensen, H. Huang, A. E. Willner, and S. Ramachandran, Science **340**, 1545 (2013).
- [12] J. Wang, J.-Y. Yang, I. M. Fazal, N. Ahmed, Y. Yan, H. Huang, Y. Ren, Y. Yue, S. Dolinar, M. Tur, and A. E. Willner, Nature Photonics **6**, 488 (2012).
- [13] H. Huang, G. Xie, Y. Yan, N. Ahmed, Y. Ren, Y. Yue, D. Rogawski, M. Tur, B. Erkmen, K. Birnbaum, S. Dolinar, M. Lavery, M. Padgett, and A. E. Willner, Optical Fiber Communication Conference/National Fiber Optic Engineers Conference 2013 (2013), paper OTh4G.5 , OTh4G.5 (2013).
- [14] G. Molina-Terriza, A. Vaziri, R. Ursin, and A. Zeilinger, Physical Review Letters **94**, 40501 (2005).
- [15] P. Picart and J.-c. Li, *Digital Holography* (John Wiley & Sons, 2013).
- [16] A. M. Ruiz, "Accurate predictive model for twisted nematic liquid crystal devices [: application for generating programmable apodizers and Fresnel lenses," (2001).
- [17] D. Preece, *Novel Uses of Spatial Light Modulators in Optical Tweezers*, Ph.D. thesis (2011).
- [18] K. Iizuka, *Elements of Photonics, In Free Space and Special Media* (John Wiley & Sons, 2002).
- [19] P. Ambs, , 1 (2001).
- [20] S. M. Kelly and M. O'Neill, Handbook of advanced electronic and ... (2000).
- [21] M. V. Berry, Journal of Optics A: Pure and Applied Optics **6**, 259 (2004).
- [22] M. J. Padgett, F. M. Miatto, M. Lavery, A. Zeilinger, and R. W. Boyd, arXiv.org , 023011 (2014), 1410.8722.
- [23] J. L. Pezvaniti and R. A. Chipman, Optics Letters **18**, 1567 (1993).
- [24] I. Moreno, J. A. Davis, C. R. Fernández-Pousa, and D. J. Franich, Optical Engineering **40**, 2220 (2001).